Materials Advances

ROYAL SOCIETY OF CHEMISTRY

PAPER

View Article Online
View Journal | View Issue

Cite this: *Mater. Adv.*, 2023, 4, 3285

Graphene-sandwiched nitrogen-enriched π-conjugated molecules as redox-active cathodes for Li-ion batteries†

Kai Chen, Xiaolan Ma, Xiaoyan Han * and Yingkui Yang*

A graphene-supported sandwiched composite (HAT-CN/Gr) was successfully fabricated through the layer-by-layer self-assembly of hexaazatriphenylenehexacarbonitrile (HAT-CN) on the surface of GO followed by thermal reduction. As applied to lithium-ion batteries (LIBs), the as-fabricated HAT-CN/Gr cathodes exhibit a superior reversal capacity (225 mA h g^{-1} at 0.05 A g^{-1}), cyclic stability (retention of 142 mA h g^{-1} at the 60th cycle) and rate capability (100 mA h g^{-1} at 2.0 A g^{-1}) due to their architectural and compositional superiority compared with pure HAT-CN cathodes. This work could give new impetus to the development of high-performance organic composite electrodes for sustainable batteries.

Received 10th June 2023,
Accepted 21st June 2023

DOI: 10.1039/d3ma00291h

rsc.li/materials-advances

1. Introduction

The energy problem of modern society is gradually coming to the fore, and people are urgently looking for low-cost, high-efficiency energy storage technologies.[1–3] In the past few years, lithium-ion batteries (LIBs) have been the most popular and commercially available energy storage devices for portable electronics because of their high operating voltage, high energy density, long cycle life, high safety, and low self-discharge.[4–6] Currently, LIBs are based primarily on lithium transition-metal oxide/phosphate cathode and graphite or Si anode materials.[7–9] However, these conventional inorganic electrode materials will suffer inevitably from the gradual depletion of available resources, increasing costs, and incalculable environmental issues, in addition to their limited practical performance which comprises low capacities and sluggish reaction kinetics.[2,10–12] Thus, the development of a novel class of energy-storage materials derived from sustainable and renewable resources is an important and much sought-after goal. Alternatively, organic electrode materials, which consist of inexpensive and sustainable elements such as C, H, O, and N provide an excellent opportunity to enhance the existing energy storage technologies.[13,14] Over the long-term perspective, future LIBs will rely on low-cost, environmentally benign, and renewable electrode materials that can be obtained directly from abundant natural resources or prepared from their derivatives.[15,16]

In the past few decades, organic electrode materials have become more and more attractive due to their inherent merits of design flexibility, fast kinetics, cost-effectiveness, lightweight nature, and environmental friendliness.[17–19] Moreover, the organic electrodes are generally not limited by the choice of counterions, making them attractive for a variety of energy storage devices,[20,21] such as metal-ion batteries,[22] redox flow batteries (RFBs),[23] Li–O_2 batteries,[24] *etc.* However, the development of organic electrodes is hindered by several problems, which include a poor cycling stability and an unsatisfactory rate performance, due to their low electronic conductivity and high dissolution in the electrolyte.[25] Accordingly, it is extremely important to alter our perspective and explore readily available and highly efficient organic electrodes to address these issues. It is generally known that the storage capability of organic electrode materials depends mainly on the molecular structure of organic compounds. Fortunately, organic electrode materials can deliver a high capacity because their molecules contain redox-enriched functional groups.[26–28] Therefore, it is essential to develop high-performance electrode materials with multiple redox-active centres by purposefully selecting or introducing macromolecular compounds at the molecular level.[29–31] So far, various strategies have been used, including optimization of the molecular structure,[32–34] the polymerization of small molecule compounds,[35,36] the adoption of solid electrolytes,[37,38] and the immobilization of redox-active materials on conducting substrates. Besides, the *in situ* combination of redox-active organic species with the graphene substrate to construct graphene-supported nanocomposites has been carried out to

Key Laboratory of Catalysis and Energy Materials Chemistry of Ministry of Education & Hubei Key Laboratory of Catalysis and Materials Science, South-Central Minzu University, Wuhan 430074, China.
E-mail: xyhan@scuec.edu.cn, ykyang@wtu.edu.cn

† Electronic supplementary information (ESI) available. See DOI: https://doi.org/10.1039/d3ma00291h

simultaneously enhance the conductivity and the utilization of active sites.[31,39,40]

Recent research has indicated that low-molecular-weight nitrogenous heterocyclic aromatic compounds with rich redox groups exhibit an excellent electrochemical activity as organic electrode materials for energy-storage technologies.[41–43] In this work, the π-conjugated aromatic macromolecule hexaazatriphenylenehexacarbonitrile (HAT-CN), which has a nitrogen-rich system, was selected for its novel organic electroactive groups. Besides, compared with traditional composite preparation methods, sonochemical methods are more favorable for the construction of graphene-based composite structures without requiring any surfactants or complex processes, where the morphology and particle size can be regulated using ultrasonic waves.[44–46] Herein, we fabricated a graphene-supported sandwich composite (HAT-CN/Gr) through a universal sonication and solvothermal process using graphene oxide (GO) and HAT-CN as the raw materials. This three-dimensional (3D) hierarchical composite structure effectively combines the advantages of both compounds, inhibits the self-aggregation or re-packing of nanocarbon materials, accelerates the redox rate, and improves the electrochemical performance of the as-fabricated materials.[47–49]

As shown in Fig. 1, the formation of the HAT-CN/Gr composites involves the initial distribution of HAT-CN molecules on the GO surfaces through π–π interactions and subsequent thermal reduction. Firstly, the HAT-CN was distributed on the graphene oxide surface *via* ultrasonic dispersion, which can avoid the mutual accumulation of molecules, helping to increase the utilization of electrochemically active sites. Then, the HAT-CN/Gr composites were obtained *via* the solvothermal reduction of graphene oxide to graphene. The addition of graphene with its inherent conductivity can improve the electron transport of the composites, and the π–π interactions between the components ensures a stable composite structure, effectively inhibiting dissolution of the organic molecule in the electrolyte. Finally, the effect of the graphene content on the morphology, structure, and the final electrochemical performance of the HAT-CN/Gr cathodes was also investigated.

2. Experimental

2.1 Synthesis of HAT-CN/Gr

First, an appropriate amount of graphene oxide (GO) was dispersed in *N*-methyl-2-pyrrolidone (NMP) *via* ultrasonication to form a uniform GO suspension. Different amounts of HAT-CN (60, 120, and 240 mg) were then added to the above dispersion system (60 mL) under constant sonication for 30 min, respectively. The resulting mixture was kept in a Teflon-lined stainless-steel autoclave at 180 °C for 12 h. The autoclave was subsequently cooled to room temperature and the product was collected by evaporating the solvent through a sand bath. The final products were dried at 120 °C under vacuum overnight and were named HAT-CN/Gr-1, HAT-CN/Gr-2, and HAT-CN/Gr-3 for the 60, 120, and 240 mg amounts of HAT-CN, respectively.

2.2 Materials characterization

Fourier transform infrared (FT-IR) spectra were recorded using a US Thermo Nicolet NEXUS 470 spectrometer in the range of 450–4000 nm. Raman spectroscopy was carried out using a Thermo Scientific DXR microscope Raman spectrometer with a laser excitation wavelength of 532 nm. X-Ray diffraction was carried out using a Rigaku/MiniFlex 600 C system in the range of 5–70°. Thermogravimetric analysis (TGA) curves were obtained using a NETZSCH (TG209F3) analyser from 40 to 700 °C at 10 °C min^{-1} under a nitrogen atmosphere. Scanning electron microscopy (SEM) was performed using a Hitachi SU8010 microscope. Transmission electron microscopy (TEM) was carried out using a Tecnai G2 20 S-TWIN microscope at 200 kV.

2.3 Electrochemical measurements

The electrochemical performance measurements were carried out using CR2032 coin cells. Lithium foil was used as the counter electrode and a Celgard-2400 microporous membrane was used as the separator. The cathode slurry was made by grinding the active material (HAT-CN or HAT-CN/Gr) with conductive carbon black (Super P) and polyvinylidene fluoride (PVDF) in a 6 : 3 : 1 weight ratio in NMP. The slurry was then uniformly coated on the surface of the aluminium foil and dried under vacuum at 80 °C overnight. The mass loading of the active materials is around 0.8 mg cm^{-2} on each electrode slice. 1.0 M LiTFSI in 1,3-dioxolane (DOL) and dimethoxymethane (DME) (v/v = 2 : 1) was used as the electrolyte. The half-cells were fabricated in an argon-filled glove box. The charge and discharge measurements were carried out using a LAND CT2001A battery testing system (Wuhan, China) in the voltage range of 1.5–3.5 V *vs.* Li^+/Li. Cyclic voltammetry (CV)

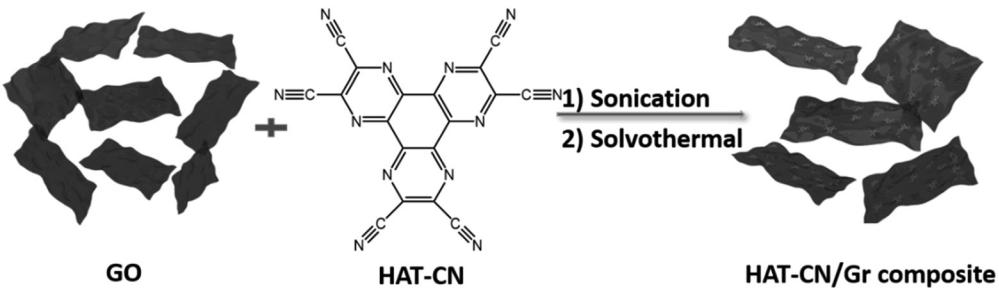

Fig. 1 Schematic illustration of the synthesis of the HAT-CN/Gr composites.

and electrochemical impedance spectroscopy (EIS) were performed at room temperature using a CHI660 electrochemical workstation.

3. Results and discussion

3.1 Structural characteristics

The morphologies of HAT-CN and its composites were investigated using SEM and TEM techniques, as shown in Fig. 2. It is observed that pure HAT-CN consists of flaky particles with a size distribution of about 1–2 μm (Fig. 2a and e). Apparently, the HAT-CN/Gr composites exhibit a lamellar structure with the HAT-CN particles confined in the graphene layers (Fig. S1b, ESI†). It is noteworthy that HAT-CN/Gr-2 (Fig. 2c and g) with an appropriate GO content shows a more uniformly dispersed morphology than HAT-CN/Gr-1 (Fig. 2b and f) and HAT-CN/Gr-3 (Fig. 2d and h). Besides, HAT-CN/Gr-1 with the lowest HAT-CN content (60 mg) presents bare graphene sheets (Fig. S1a, ESI†), and HAT-CN/Gr-3 with the highest HAT-CN content (240 mg) shows a serious aggregation phase of the HAT-CN particles due to the limited nucleation sites (Fig. S1c, ESI†).

The chemical structures of pure HAT-CN and the HAT-CN/Gr composites were further examined using spectroscopy techniques and thermogravimetric analysis (Fig. 3). As shown in the FT-IR spectra (Fig. 3a), the characteristic absorption peaks at 1634, 1560, and 1393 cm^{-1} correspond to the C═N, C═C, and C–N stretching vibration peaks, respectively, in pure HAT-CN, while the characteristic peak of C≡N at 2240 cm^{-1} was not evident in the composites, which can be attributed to the high graphene content. Furthermore, the strong diffraction peak of GO (8.6°) disappeared after solvothermal reduction and was replaced by a broad peak at about 25° in the XRD pattern (Fig. 3b), indicating that the oxygen-containing functional groups were effectively removed after the reduction and the structural defects of GO were repaired. The diffraction peaks of the HAT-CN/Gr composites are significantly weakened, which can be ascribed to the re-assembly between HAT-CN and the Gr nanosheets *via* π–π interactions during the ultrasonication process. The relatively broad diffraction peaks of the HAT-CN/Gr composites demonstrate the presence of HAT-CN molecules between the graphene layers, resulting in a poor degree of order. Besides, in their Raman spectra (Fig. 3c), all the HAT-CN/Gr composites exhibit similar D (*ca.* 1340 cm^{-1}) and G (*ca.* 1575 cm^{-1}) bands, which correspond to the disordered structure and the sp^2-hybridized configuration, respectively. The Raman shift of the G peak (HAT-CN/Gr-3) to a lower frequency (1570 cm^{-1}) compared with pure Gr (1586 cm^{-1}) indicates that the charges on the heteroaromatic rings of HAT-CN are partially transferred to the graphene layers due to the strong π–π interactions between HAT-CN and graphene.[50,51] The loading amount of HAT-CN in the composites can be estimated using TGA (Fig. 3d) and elemental analysis (Table S1, ESI†). The TGA trace of bare HAT-CN shows a clear weight loss after 500 °C, and at 700 °C a weight of 22.6% is retained due to the dissociation and carbonization of the macromolecular chains. By contrast, the resultant HAT-CN/Gr composites demonstrate high thermal stability while maintaining a large residual weight (50–60%) due to carbonization of the graphene component. Meanwhile, the measured N contents in HAT-CN, HAT-CN/Gr-1, HAT-CN/Gr-2, and HAT-CN/Gr-3 were 42.36, 13.99, 17.64, and 21.85 wt%, respectively. Therefore, the loading amounts of HAT-CN in the composites are calculated to be about 33.0 wt% in HAT-CN/Gr-1, 41.6 wt% in HAT-CN/Gr-2, and 49.3 wt% in HAT-CN/Gr-3.

3.2 Lithium-storage performance

To reveal the electrochemical performance and storage mechanism, pure HAT-CN and the HAT-CN/Gr composites as cathodes were evaluated *via* a series of electrochemical

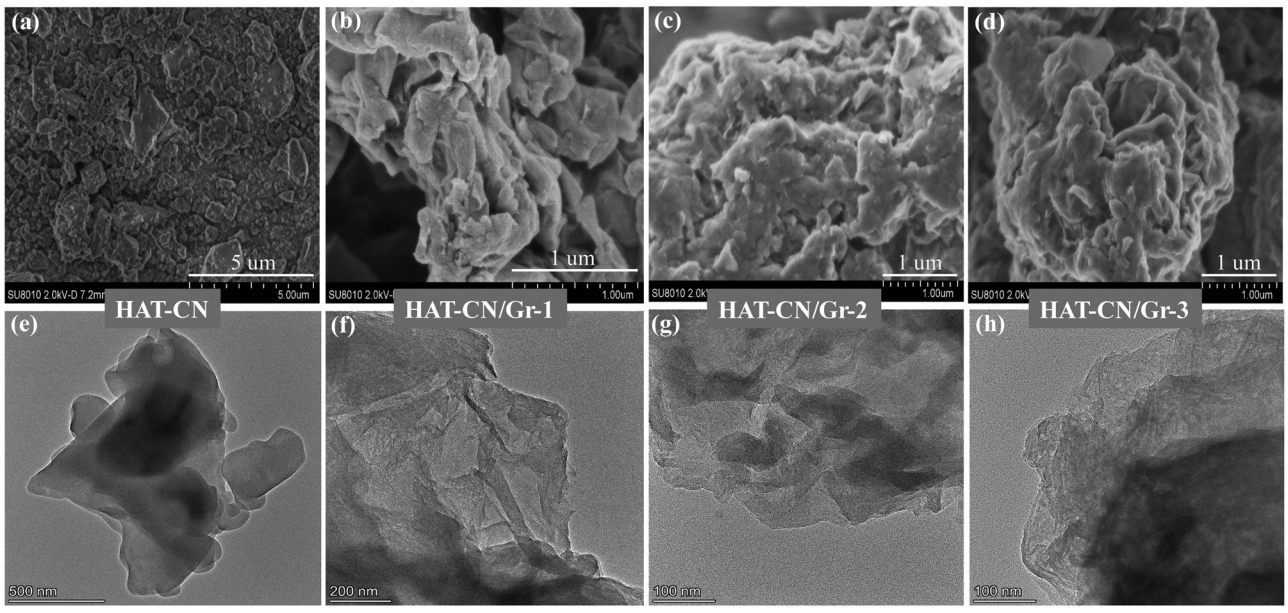

Fig. 2 (a)–(d) SEM and (e)–(h) TEM images of HAT-CN and the HAT-CN/Gr composites.

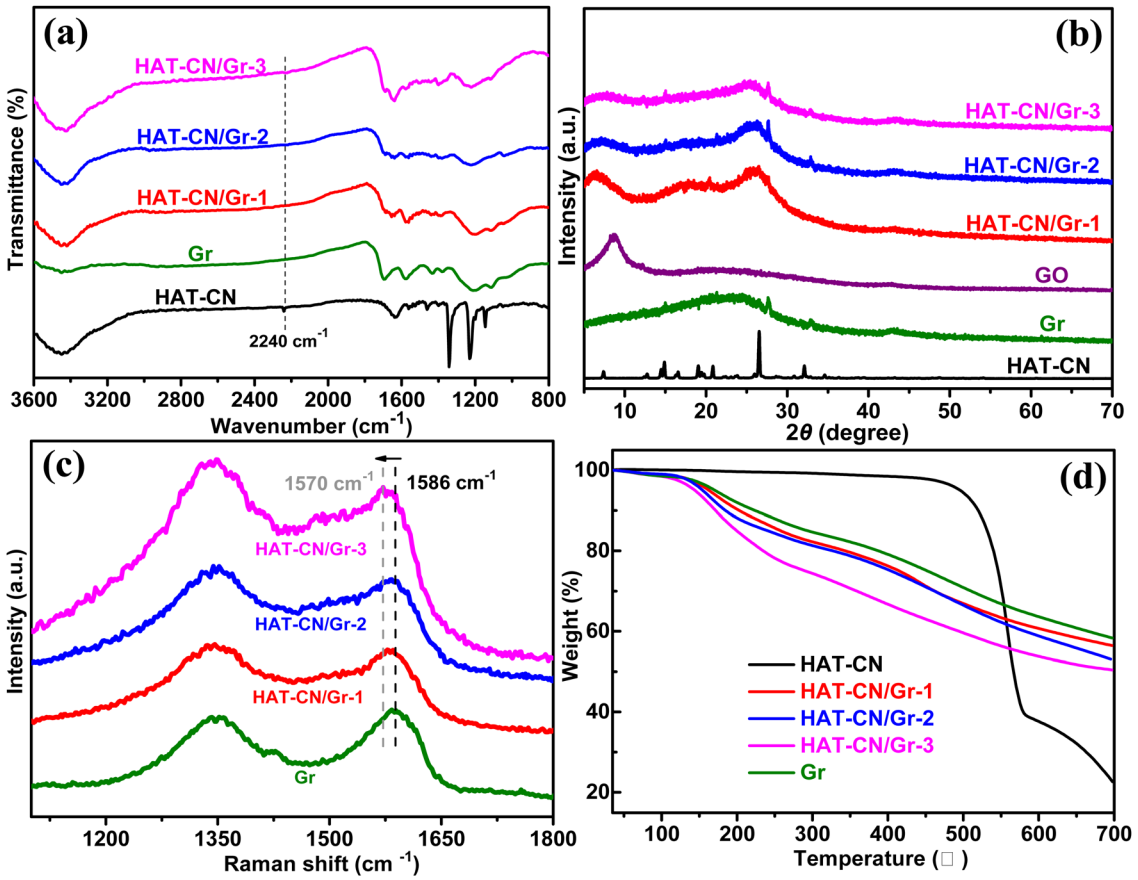

Fig. 3 (a) FT-IR spectra, (b) XRD patterns, (c) Raman spectra, and (d) TGA curves for HAT-CN, Gr, GO, and the HAT-CN/Gr composites.

techniques. Fig. 4a shows the cyclic voltammogram (CV) curves of the HAT-CN/Gr-2 electrode between 1.5 and 3.5 V at a scan rate of 0.5 mV s^{-1}, which exhibits two clear broad peaks, demonstrating the multi-step redox reactions during the charging/discharging processes and the highly reversible nature of the electrode.[52,53] The broad peaks at 2.0–2.2 V originate from the first three redox active sites of the hexaazatrinaphthalene (HATN) unit, and the broad peaks at 2.6–2.9 V correspond to the last three redox couples of the HATN unit;[30,53] the Li storage mechanism and corresponding equations are shown in Fig. S2 (ESI†). Besides, such CV profiles can be clearly identified in the HAT-CN (Fig. S3a, ESI†), HAT-CN/Gr-1 (Fig. S3b, ESI†), and HAT-CN/Gr-3 cathodes (Fig. S3c, ESI†). The charge/discharge profile of the HAT-CN/Gr-2 cathode is shown in Fig. 4b, which presents two sloping plateaus at about 2.25 and 2.75 V, tallying with the CV results (Fig. 4a). Careful observation of the typical CV curves for the stable 2nd cycle (Fig. S4a, ESI†) reveals that all the HAT-CN/Gr cathodes exhibit stronger redox peaks

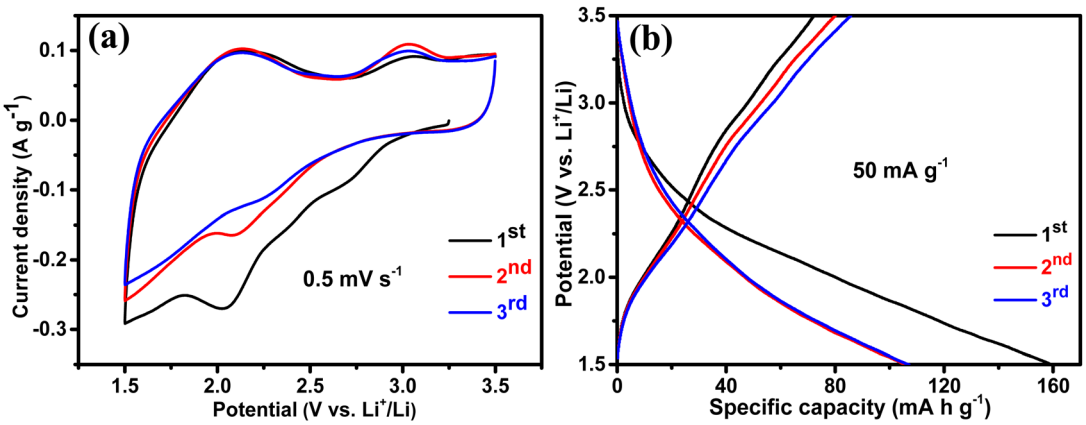

Fig. 4 Typical CV curves (a) and charge/discharge voltage profiles (b) of the HAT-CN/Gr-2 cathode for the first three cycles.

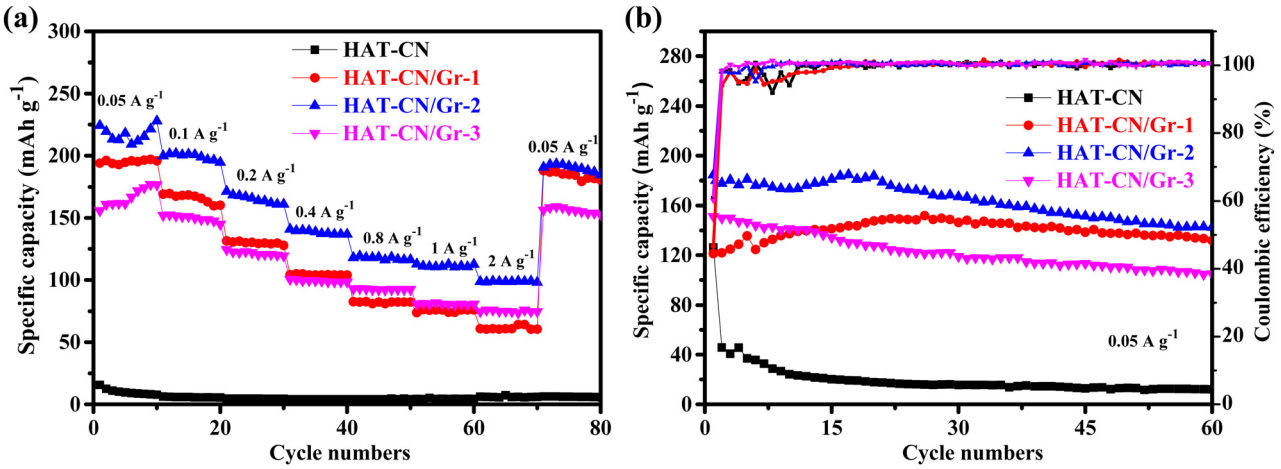

Fig. 5 Rate performance (a) and cycling stability (b) for HAT-CN and the HAT-CN/Gr cathodes.

compared with pure HAT-CN due to the graphene-supported conductive networks and compact sandwich π–π packing that is capable of boosting redox kinetics and ion diffusion, which is identified by the increasing reversible capacity in Fig. S4b (ESI†). Furthermore, the graphene-supported sandwich structure endows the HAT-CN/Gr composites with higher stable capacities (over 70 mA h g^{-1}) compared with pure HAT-CN (below 40 mA h g^{-1}) (Fig. 4b and Fig. S3d–f, ESI†), which is due to the improved redox activity and electrochemical utilization rate of the HAT-CN molecules. In particular, the approximate overlap of the charge/discharge profiles between the 2nd and 3rd cycles for the HAT-CN/Gr cathodes (Fig. 4b and Fig. S3e and f, ESI†) suggests the strong stability and high reversibility of lithium uptake and release during the charge/discharge processes.

The rate and cycling performances of the HAT-CN-based cathodes were also tested (Fig. 5). As shown in Fig. 5a, apparently, pure HAT-CN always delivers the lowest reversible capacities (<20 mA h g^{-1}) whereas HAT-CN/Gr-2 possesses the highest reversible capacities at each rate (225 mA h g^{-1} at 0.05 A g^{-1} and 200 mA h g^{-1} at 0.1 A g^{-1}). Typically, at an elevated rate of 2.0 A g^{-1}, pure HAT-CN retains a much lower capacity (6 mA h g^{-1}) compared with HAT-CN/Gr-1 (61 mA h g^{-1}), HAT-CN/Gr-2 (100 mA h g^{-1}), and HAT-CN/Gr-3 (75 mA h g^{-1}). Moreover, after returning to 0.05 A g^{-1}, each of the HAT-CN/Gr composite cathodes almost recovers its initial capacity, suggesting their excellent rate capabilities. In particular, HAT-CN/Gr-2 with a suitable loading level of GO exhibits the best rate performance, which can be attributed to the uniform sandwich structure that is capable of providing abundant efficient active sites, as confirmed by the cycling performance in Fig. 5b. As shown in Fig. 5b, the HAT-CN cathode presents an initial charge capacity of 123 mA h g^{-1} and retains only 12 mA h g^{-1} after 60 cycles, indicating a poor cycling stability. By contrast, HAT-CN/Gr-2 delivers an initial capacity of up to 185 mA h g^{-1} and maintains a reversible capacity of 142 mA h g^{-1} at the 60th cycle, in good accordance with the above results. Besides, it is worth noting that pure graphene contributes a very low capacity because the reversible capacity is very low for the same voltage range (Fig. S5, ESI†).

The electron transport and ion diffusion kinetics were further revealed *via* EIS. Each of the HAT-CN/Gr cathodes

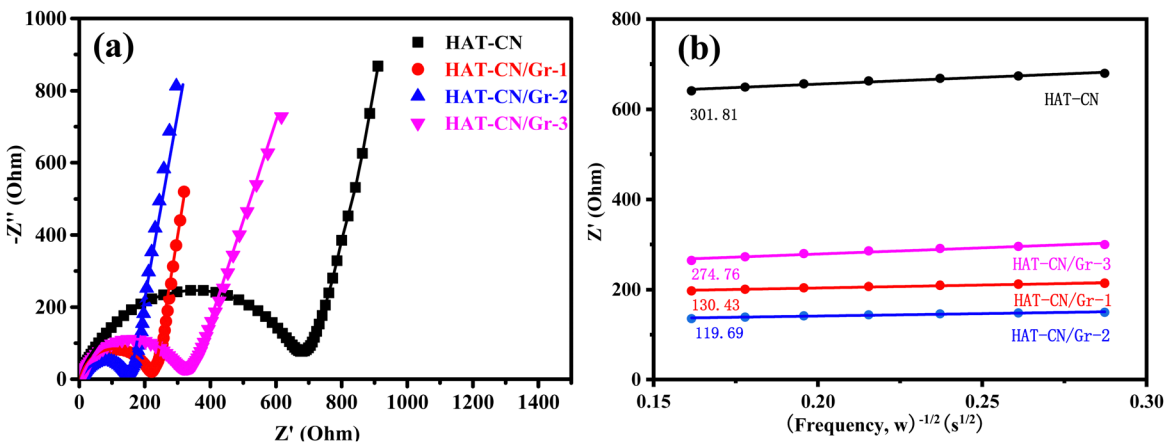

Fig. 6 Nyquist plots (a) and linear plots of the real parts of complex impedance *vs.* $\omega^{-1/2}$ (b) for pure HAT-CN and the HAT-CN/Gr composite cathodes.

exhibits a lower charge transfer resistance (R_{ct}) than pure HAT-CN due to the enhanced electronic conductivity contributed by Gr (Fig. 6a). Typically, the HAT-CN/Gr-2 cathode possesses the lowest charge transfer resistance (153.3 Ω) among HAT-CN/Gr-1 (220.8 Ω), HAT-CN/Gr-3 (322.9 Ω), and HAT-CN (680.1 Ω). As a consequence, HAT-CN/Gr-2 also shows a smaller value for the ion-diffusion resistance (σ; Fig. 6b) compared with HAT-CN/Gr-1, HAT-CN/Gr-3, and HAT-CN, implying its faster Li-ion diffusion throughout the composite electrode. These kinetic behaviors are ascribable to the multifunctionality of graphene. Conductive graphene nanosheets are closely stacked with HAT-CN molecules to build a stable graphene-sandwiched network that enables efficient electron transport, and a large specific surface area, resulting in fast electrolyte infusion and ion diffusion. Beyond that, the strong π–π interaction between the Gr and HAT-CN layers is favourable for effective electron transport and structural stability in deeply charged/discharged states, thus rendering reversible and stable redox reactions of the composite cathodes.

4. Conclusions

A series of graphene/nitrogen-enriched composites (HAT-CN/Gr) was readily achieved from graphene oxide (GO) and hexaazatriphenylenehexacarbonitrile (HAT-CN) *via* a sonication process in combination with subsequent thermal treatment. Conductive graphene nanosheets (Gr) derived from the hydrothermal reduction of GO are fully covered by multi-electron redox-active HAT-CN lamellae. The optimum as-fabricated HAT-CN/Gr cathode delivers a high reversible capacity of 225 mA h g^{-1} at 0.05 A g^{-1} and retains a rate capability of 100 mA h g^{-1} at 2.0 A g^{-1}, and a cyclic stability of 142 mA h g^{-1} after 60 cycles. This excellent electrochemical performance can be attributed to the synergistic merits of the sandwich construction, which consists of highly conductive graphene and π-conjugated redox-active molecules. Firstly, the highly conjugated HAT-CN layers contain abundant aromatic C/N atoms, which provide multi-electron active sites. Secondly, the strong π–π interactions between the graphene nanosheets and the HAT-CN layers enable intimate contact for the sandwich network, enabling fast electron/ion transport and efficient electrochemical reactions. This work will provide new insights into the construction of graphene-based sustainable organic electrodes for the next generation of low-cost and high-performance rechargeable batteries.

Conflicts of interest

There are no conflicts to declare.

Acknowledgements

This work was supported by the National Natural Science Foundation of China (52173091 and 51973235), Hubei Provincial Natural Science Foundation of China (2021CFA022), and Fundamental Research Funds for Central Universities, South-Central Minzu University (CZQ21011).

References

1 A. Masias, J. Marcicki and W. A. Paxton, *ACS Energy Lett.*, 2021, **6**(2), 621–630.
2 D. Larcher and J. M. Tarascon, *Nat. Chem.*, 2015, **7**(1), 19–29.
3 T. Kim, W. Song, D.-Y. Son, L. K. Ono and Y. Qi, *J. Mater. Chem. A*, 2019, **7**(7), 2942–2964.
4 J. Xie and Y.-C. Lu, *Nat. Commun.*, 2020, **11**(1), 2499.
5 Z. Fang, J. Wang, H. Wu, Q. Li, S. Fan and J. Wang, *J. Power Sources*, 2020, **454**, 227932.
6 M. Weiss, R. Ruess and J. Kasnatscheew, *Adv. Energy Mater.*, 2021, **11**(33), 2101126.
7 P. Simon, Y. Gogotsi and B. Dunn, *Science*, 2014, **343**(6176), 1210–1211.
8 A. Manthiram and J. B. Goodenough, *Nat. Energy*, 2021, **6**(8), 844–845.
9 S. Chae, M. Ko, K. Kim, K. Ahn and J. Cho, *Joule*, 2017, **1**(1), 47–60.
10 P. Poizot, J. Gaubicher, S. Renault, L. Dubois, Y. Liang and Y. Yao, *Chem. Rev.*, 2020, **120**(14), 6490–6557.
11 M. K. Tran, M.-T. F. Rodrigues, K. Kato, G. Babu and P. M. Ajayan, *Nat. Energy*, 2019, **4**(4), 339–345.
12 Y. Yang, E. G. Okonkwo, G. Huang, S. Xu, W. Sun and Y. He, *Energy Storage Mater.*, 2021, **36**, 186–212.
13 X. Wu, X. Feng, J. Yuan, X. Yang, H. Shu, C. Yang, Z. Liu, J. Peng, E. Liu, S. Tan and P. Gao, *Energy Storage Mater.*, 2022, **46**, 252–258.
14 D. M. Heard and A. J. J. Lennox, *Angew. Chem., Int. Ed.*, 2020, **59**(43), 18866–18884.
15 J. Jiang, J. Zhu, W. Ai, Z. Fan, X. Shen, C. Zou, J. Liu, H. Zhang and T. Yu, *Energy Environ. Sci.*, 2014, **7**(8), 2670–2679.
16 Y. Lu and J. Chen, *Nat. Rev. Chem.*, 2020, **4**(3), 127–142.
17 N. Goujon, N. Casado, N. Patil, R. Marcilla and D. Mecerreyes, *Prog. Polym. Sci.*, 2021, **122**, 101449.
18 Q. Zhang, Y. Dou, Q. He, S. Deng, Q. Huang, S. Huang and Y. Yang, *Energy Environ. Mater.*, 2022, **5**(4), 1037–1059.
19 T. B. Schon, B. T. Mcallister, P.-F. Li and D. S. Seferos, *Chem. Soc. Rev.*, 2016, **45**(22), 6345–6404.
20 C. Han, H. Li, R. Shi, T. Zhang, J. Tong, J. Li and B. Li, *J. Mater. Chem. A*, 2019, **7**(41), 23378–23415.
21 J. Wang, H. Yao, C. Du and S. Guan, *J. Power Sources*, 2021, **482**, 228931.
22 P. Luo, C. Zheng, J. He, X. Tu, W. Sun, H. Pan, Y. Zhou, X. Rui, B. Zhang and K. Huang, *Adv. Funct. Mater.*, 2022, **32**(9), 2107277.
23 P. V. Kamat, K. S. Schanze and J. M. Buriak, *ACS Energy Lett.*, 2017, **2**(6), 1368–1369.
24 H.-D. Lim, B. Lee, Y. Bae, H. Park, Y. Ko, H. Kim, J. Kim and K. Kang, *Chem. Soc. Rev.*, 2017, **46**(10), 2873–2888.
25 D. Xu, M. Liang, S. Qi, W. Sun, L.-P. Lv, F.-H. Du, B. Wang, S. Chen, Y. Wang and Y. Yu, *ACS Nano*, 2021, **15**(1), 47–80.

26 J. Hong, M. Lee, B. Lee, D. H. Seo, C. B. Park and K. Kang, *Nat. Commun.*, 2014, **5**, 5335.
27 E. Castillo-Martínez, J. Carretero-González and M. Armand, *Angew. Chem.*, 2014, **53**(21), 5341–5345.
28 S. Xu, G. Wang, B. P. Biswal, M. Addicoat, S. Paasch, W. Sheng, X. Zhuang, E. Brunner, T. Heine, R. Berger and X. Feng, *Angew. Chem.*, 2019, **58**(3), 849–853.
29 H. Wang, C.-J. Yao, H.-J. Nie, K.-Z. Wang, Y.-W. Zhong, P. Chen, S. Mei and Q. Zhang, *J. Mater. Chem. A*, 2020, **8**(24), 11906–11922.
30 J. Wang, C. S. Chen and Y. Zhang, *ACS Sustainable Chem. Eng.*, 2018, **6**(2), 1772–1779.
31 W. Ai, Z. Luo, J. Jiang, J. Zhu, Z. Du, Z. Fan, L. Xie, H. Zhang, W. Huang and T. Yu, *Adv. Mater.*, 2014, **26**(35), 6186–6192.
32 Y. Liang, P. Zhang, S. Yang, Z. Tao and J. Chen, *Adv. Energy Mater.*, 2013, **3**(5), 600–605.
33 Y. Morita, S. Nishida, T. Murata, M. Moriguchi, A. Ueda, M. Satoh, K. Arifuku, K. Sato and T. Takui, *Nat. Mater.*, 2011, **10**(12), 947–951.
34 Q. Zhang, X. Cui, S. Hao, Q. Zhang, Z. Guo, H. Li, Z. Lin and Y. Yang, *Mater. Today*, 2021, **50**, 170–198.
35 T. Nokami, T. Matsuo, Y. Inatomi, N. Hojo, T. Tsukagoshi, H. Yoshizawa, A. Shimizu, H. Kuramoto, K. Komae, H. Tsuyama and J.-I. Yoshida, *J. Am. Chem. Soc.*, 2012, **134**(48), 19694–19700.
36 Z. Song, Y. Qian, M. L. Gordin, D. Tang, T. Xu, M. Otani, H. Zhan, H. Zhou and D. Wang, *Angew. Chem., Int. Ed.*, 2015, **54**(47), 13947–13951.
37 P. Zhou, J. Wang, F. Cheng, F. Li and J. Chen, *Chem. Commun.*, 2016, **52**(36), 6091–6094.
38 Z. Zhu, M. Hong, D. Guo, J. Shi, Z. Tao and J. Chen, *J. Am. Chem. Soc.*, 2014, **136**(47), 16461–16464.
39 B. Genorio, K. Pirnat, R. Cerc-Korosec, R. Dominko and M. Gaberscek, *Angew. Chem.*, 2010, **49**(40), 7222–7224.
40 A. Jaffe, A. Saldivar Valdes and H. I. Karunadasa, *Chem. Mater.*, 2015, **27**(10), 3568–3571.
41 J. Wu, X. Rui, G. Long, W. Chen, Q. Yan and Q. Zhang, *Angew. Chem., Int. Ed.*, 2015, **54**(25), 7354–7358.
42 Q. Liu, Z. Xiao, X. Cui, S. Deng, Q. He, Q. Zhang, Z. Lin and Y. Yang, *J. Mater. Chem. A*, 2021, **9**(11), 6962–6970.
43 T. Gu, M. Zhou, B. Huang, S. Cao, J. Wang, Y. Tang, K. Wang, S. Cheng and K. Jiang, *Chem. Eng. J.*, 2019, **373**, 501–507.
44 K. G. Lee, J. M. Jeong, S. J. Lee, B. Yeom, M. K. Lee and B. G. Choi, *Ultrason. Sonochem.*, 2015, **22**, 422–428.
45 X. Han, Z. Huang, C. He, Q. Zhang, X. Zhang and Y. Yang, *J. Appl. Electrochem.*, 2019, **49**(11), 1133–1142.
46 X. Han, R. Li, S. Qiu, X. Zhang, Q. Zhang and Y. Yang, *RSC Adv.*, 2019, **9**(11), 5942–5947.
47 C. Tang, Q. Zhang, M.-Q. Zhao, J.-Q. Huang, X.-B. Cheng, G.-L. Tian, H.-J. Peng and F. Wei, *Adv. Mater.*, 2014, **26**(35), 6100–6105.
48 R. Zhang, Y. Dong, M. A. Al-Tahan, Y. Zhang, R. Wei, Y. Ma, C. Yang and J. Zhang, *J. Energy Chem.*, 2021, **60**, 85–94.
49 J. Hu, L. Sun, F. Xie, Y. Qu, H. Tan, X. Shi, J. Qian, K. Wang and Y. Zhang, *J. Mater. Chem. A*, 2022, **10**(40), 21590–21602.
50 A. M. Rao, P. C. Eklund, S. Bandow, A. Thess and R. E. Smalley, *Nature*, 1997, **388**(6639), 257–259.
51 Z. Liu, K. Parvez, R. Li, R. Dong, X. Feng and K. Müllen, *Adv. Mater.*, 2015, **27**(4), 669–675.
52 W. Huang, Z. Zhu, L. Wang, S. Wang, H. Li, Z. Tao, J. Shi, L. Guan and J. Chen, *Angew. Chem., Int. Ed.*, 2013, **52**(35), 9162–9166.
53 C. Peng, G.-H. Ning, J. Su, G. Zhong, W. Tang, B. Tian, C. Su, D. Yu, L. Zu, J. Yang, M.-F. Ng, Y.-S. Hu, Y. Yang, M. Armand and K. P. Loh, *Nat. Energy*, 2017, **2**(7), 17074.